
Calcaneus Radiograph Analysis System: Rotation-Invariant Landmark Detection, Calcaneal Angle Measurement and Fracture Identification

Jia Guo¹, Huiqi Li^{1*}, Junxian Chen¹, Wei Wang², Huanxin Yan³, Hailin Xu^{4*}

¹Beijing Institute of Technology, Beijing 100081, China

²The First Affiliated Hospital of Jinzhou Medical University, Jinzhou 121001, China

³Zhejiang University of Science & Technology, Zhejiang 310032, China

⁴Peking University People's Hospital, Beijing 100044, China

Abstract. Calcaneus is the largest tarsal bone to withstand the daily stresses of weight bearing. The calcaneal fracture is the most common type in the tarsal bone fractures. After a fracture is suspected, plain radiographs should be taken first. Bohler's Angle (BA) and Critical Angle of Gissane (CAG), measured by four anatomic landmarks in lateral foot radiograph, can aid operative restoration of the fractured calcaneus and fracture diagnosis and assessment. The aim of this study is to develop a system to automatically locate four anatomic landmarks and measure BA and CAG for fracture assessment. To solve the problem of fickle rotation of calcaneus, we proposed a coarse-to-fine Rotation-Invariant Regression-Voting (RIRV) landmark detection method based on Supported Vector Regression (SVR) and Scale Invariant Feature Transform (SIFT) patch descriptor. By implementing a novel normalization approach to convert displacements into coordinates of oriented feature patches, our method is explicit rotation-invariance comparing with traditional regressive method. A multi-stream CNN structure with multi-region input is designed to screen calcaneus fracture. The input ROIs of multi-stream CNN are normalized by detected landmarks to uniform view, orientation and scale. The advantage of our approach is the usage of landmarks using prior knowledge to normalize the inputs of CNN so as to improve the efficiency of CNN. Experiments show that our CNN can accurately identify the fractures with sensitivity of 95.21% and specificity of 95.32%.

Keywords: Calcaneus Fractures; Calcaneus Radiograph; Landmark Detection; Fracture Detection; Rotation Invariance; Convolutional Neural Network.

1. Introduction

Calcaneus, also known as heel bone, is the largest tarsal bone to withstand the daily stresses of weight bearing. The calcaneal fracture is the most common type in the tarsal bone fractures, accounting for 2% of all fractures and 60% of tarsal bone fracture [1]. Imaging of a suspected fracture usually begins with plain radiographs. If plain radiographs are not conclusive, further investigations with magnetic resonance imaging (MRI), computed tomography (CT) or nuclear medicine bone scan are required for diagnosis. Though CT represents a promising tool for surgical decision, plain X-ray radiograph is a better screening method due to its low-cost, convenience and less exposure to beams. Bohler's Angle (BA) [2] of the calcaneus has been used since 1931 to aid operative restoration of the fractured calcaneus and fracture diagnosis. Another angle that has been used to diagnose calcaneus fractures is the Critical Angle

*Huiqi Li (E-mail: huiqili@bit.edu.cn) and Hailin Xu (E-mail: hailinxu66@qq.com) are the corresponding professors.

of Gissane (CAG) [3]. While the CAG has largely been abandoned in routine outcome reporting for patients with calcaneal fracture, BA remains a commonly used gauge for injury severity and a standard by which radiographic outcome after surgery is determined [4]. There is overwhelming evidence that restoring Bohler's angle to near normal after fracture indicates better outcomes [5] [6] [7].

BA can be measured as the angle between two intersecting lines: a line connecting the posterior tuberosity of calcaneus and the apex of the posterior facet of calcaneus and a line between the apex of the posterior facet and the apex of the anterior process of calcaneus as illustrated in Figure 1(a). CAG is formed by two strong cortical struts that extend laterally and form an obtuse angle directly inferior to the lateral process of the talus. CAG can be measured as the angle between lateral border of the posterior facet and lateral border of the anterior facet as illustrated in Figure 1(b). The normal range for BA and CAG in the atraumatic adult calcaneus has been quoted between roughly $20 - 45^\circ$ [2] and $90 - 150^\circ$ respectively [2]. The measurement of BA and CAG rely on the location of four anatomical landmarks L_1 , L_2 , L_3 and L_4 . Therefore, the accuracy localization of landmarks is the key to the measurement of calcaneal angles.

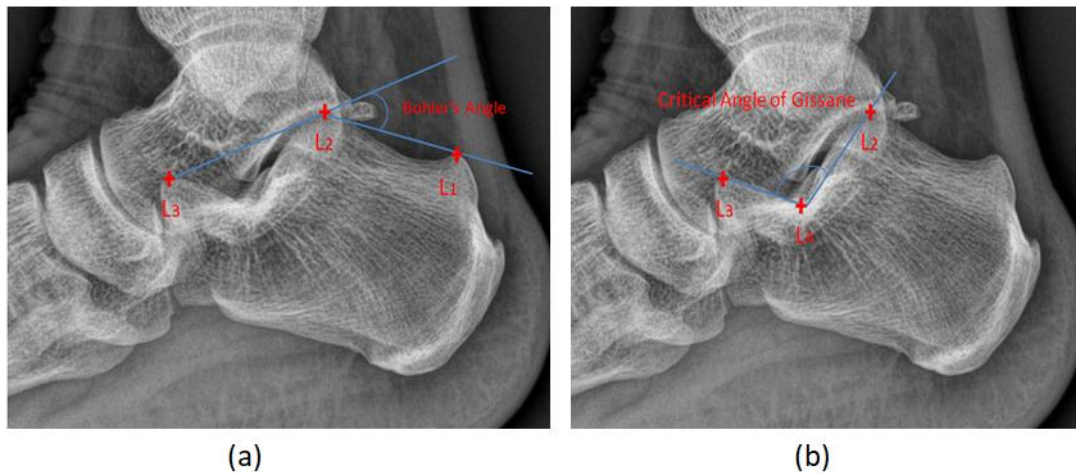


Figure 1 BA and CAG in lateral calcaneus radiograph. (a) Bohler's Angle. (b) Critical Angle of Gissane.

The localization of anatomical landmarks is an important and challenging step in the clinical workflow for therapy planning and intervention. The algorithms for different applications have been well investigated in the past decades, including spinal flexibility [8], kneealignment angles [9], cephalogram analysis [10] [11] and so on. A number of approaches have been developed for landmarks or key-point localization. A common approach to localize multiple landmarks is to combine multiple independent localizers for individual landmarks with a statistical shape model regularizer, e.g., Active Shape Models (ASMs) and Constrained Local Models (CLMs). Classifier-based anatomical landmark localization classifies the positions of selected interest points [12]. Regression-voting-based approaches, as alternatives, have become the mainstream, such as [13] and [14]. Currently, deep learning algorithms, in particular convolutional networks, have rapidly become a methodology of choice for analyzing medical images. Several approaches have been proposed to detect anatomical landmarks in both 2D and 3D medical CR and MRI images [15][16]. Classifiers can only predict whether the tested location is the target location or not. To achieve high accuracy, the candidate points have to be precise dense which is not possible for purely classifier-based approaches. Approaches that use local image information and regression based techniques, on the other hand, can provide much more detailed information. Work on Hough Forests [17] has shown that objects can be effectively located by pooling votes from Random Forest (RF) [18] regressors, and that facial feature points can be accurately located following a similar

approach using kernel SVM-based regressors [19].

Some work [20] indicates that rotation invariance might not be necessary in most medical contexts; however, the lateral foot radiographs are not among them due to fickle variance of rotation due to the different postures of patient and condition of X-ray machine as shown in Figure 2. Most approach based on regressive localization is not explicit rotationally invariant as opposed to classified localization such as [12]. When implement regression-voting based method in datasets with bigger rotations, it is suggested to initially use a 2D registration algorithm such as [21] in order to roughly align the images between each other before analysis [22]. In addition, statistical shape model is unnecessary in the context of calcaneal radiograph because of the small number of landmarks, only four, and the big difference of point shapes between normal and fractured calcaneus.

Convolution neural network (CNN) is a type of machine learning method that produces state-of-art performance on image recognition tasks; and it has been well performed in medical image processing. There have been many attempts to use CNN to detect bone fractures [23] [24]. Previous two computer-assisted diagnosis of calcaneus fracture concentrates on calcaneus CT [25] [26]. For calcaneus radiograph, it is very challenging for fracture identification because of the inconsistent rotation and view, the complex anatomy and the lack of medical information comparing to CT.

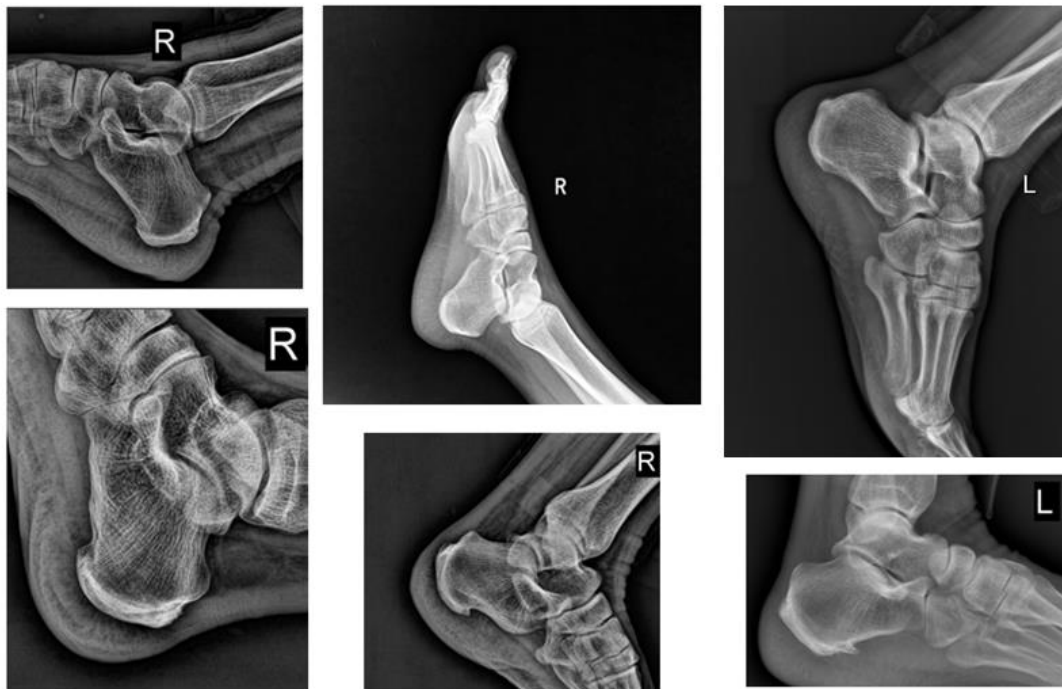


Figure 2 Rotation and view variance in lateral foot radiograph

In this paper, we present a new analysis system of calcaneus fracture detection in radiographs, including landmarks detection, measurement of BA and CAG and automatic fracture identification. Firstly, we proposed a coarse-to-fine Rotation-Invariant Regression-Voting (RIRV) method based on Supported Vector Regression (SVR) [27] and Scale Invariant Feature Transform (SIFT) [28] patch descriptor. Secondly, the locations of anatomic landmarks are used to calculate BA and CAG which can be used by orthopedists to assess the condition of fracture. Thirdly, we proposed a fracture identification method based on multi-stream CNN with multi-region calcaneus as input. Our contribution can be summarized as : (1) In the RIRV, we normalize the regressive displacement by the scale and orientation of each SIFT patch, which results in the explicit scale-rotation invariance without data augmentation or rough alignment; (2) we designed a novel screening method, half-path double voting (HDPV), to remove

unconfident voting candidates caused by far, noisy or blurry image patches; (3) we employed multi-stage coarse-to-fine strategy, so that the latter stage can make use of the rotation and scale information obtained from the detection of previous stage. (4) In multi-stream CNN, we make use of the landmarks' location as medical prior knowledge in fracture identification. The input ROIs of multi-stream CNN are normalized by the result of detected landmarks to uniform view, orientation and scale so that satisfactory performance of multi-stream CNN can be obtained with a small number of training data.

2. Method

The flow chart of our calcaneus radiograph analysis system is shown in Figure 3. First, the radiographs with toe-right calcaneus are identified and automatically flipped to toe-left before landmark detection because our method is not flip-invariant. The automatic toe-right identification is based on the flip-variant characteristic of RIRV, which is discussed in 2.2.5. Second, four landmarks are localized by RIRV detection method. The locations of landmarks are then used to calculate BA and CAG for clinical assessment. Fractures or normal can be identified by multi-stream CNN structure with multi-region input, which is cropped and rotated according to the locations of landmarks.

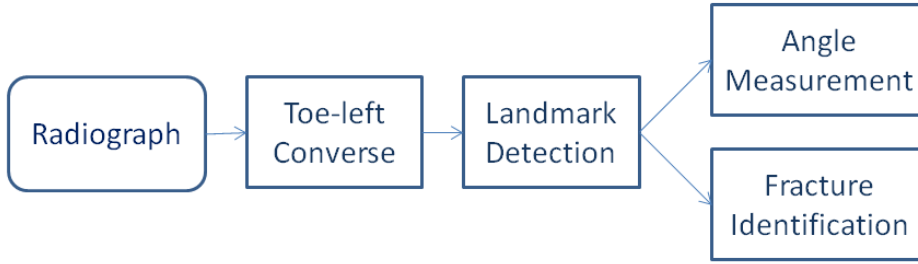


Figure 3 Flow chart of the calcaneus radiograph analysis system.

2.1 Rotation-Invariant Regression-Voting (RIRV)

2.1.1 Restrictions of Regression Voting and Its Improvement

In traditional regression-voting approach, we train a set of regressors for every landmark from a set of radiographs. For each landmark $L_i(x, y)$, $i = 1, 2, 3, 4$, N SIFT patch features $\mathbf{f}_j(\mathbf{p}(x, y, s, \theta))$, $j = 1, 2 \dots N$ are extracted from a set of random image patches $\mathbf{p}_j(x, y, s, \theta)$ sampled in the ROI where x , y , s and θ are x coordinate of patch center, y coordinate of patch center, scale and orientation of the image patch, respectively. Next, the set of displacements $\mathbf{d}_j(x, y)$ from the center of random patches to the landmark ground truth are calculated. Then a regressor $\delta = \mathbf{TR}(\mathbf{f}_j, \mathbf{d}_j)$ is trained to predict the relative displacements $\bar{\mathbf{d}}_j$ from \mathbf{p}_j to L_i . The displacements can be used to predict most likely position of the landmark based on simple voting of candidate $\mathbf{c}_j = \mathbf{p}_j + \bar{\mathbf{d}}_j$. The regressive displacement is illustrated in Figure 4(a); the left eye is the target points.

However, though SIFT features are extracted with scale and orientation, the displacement is calculated on the base of image coordinate: x represents pixel column and y represents pixel row, which is variant to

the rotation of calcaneus. The regressive displacements learned from Figure 4(a) are performed on a rotated object and a scaled object, as illustrated in Figure 4(b) and Figure 4(c). Though in most medical application when the rotation and scale of object are controlled in fine extent and the training set can be artificially inflated by randomly rotating and perturbing the training data, data augmentation can hardly deal with calcaneal radiograph in such dominant rotation variance.

Therefore, in our method, we normalize the regressive displacement \mathbf{d}_j to $\mathbf{d}^{norm}_j(x^{norm}, y^{norm})$ in coordinate of each image patch \mathbf{p}_j by the scale and orientation of the image patch in the first stage; and by the location of L_1 and L_2 in the second, third and fourth stage, which result in the explicit scale-rotation invariance without need of image augmentation.

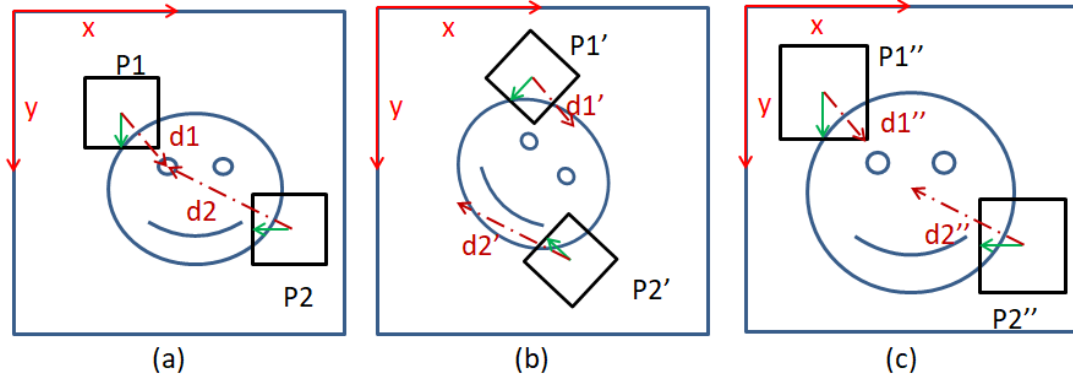


Figure 4 Regressive displacement relationship. Black squares represent sift patches and green arrows are the orientations of the patches. Red arrows are image coordinate. Crimson dash lines are the displacement from the center of patches to the left eye. (a) Regressive displacement learned in original image. (b) The learned regressive displacement performing on rotated image. (c) The learned regressive displacement performing on scaled image.

2.1.2 SIFT Feature Descriptor.

SIFT descriptor is used to represent local feature for corner points in the field of image matching, which was developed by Lowe in 2004 [28]. The algorithm of SIFT feature extraction includes four steps: scale-space extrema detection: potential key points are extracted in scale-space by using difference-of-Gaussian image pyramids; key point localization: determine the location and scale of the key point; orientation assignment: the orientation θ is assigned to the key point to provide invariance to rotation; and generating key point descriptor: the local gradient is calculated in the selected scale which will provide invariance to shape distortion.

The advantage of SIFT features to represent the key points is affine invariant and robust to illumination change for images. This feature extraction method has been widely used in the fields of image matching and registration.

In this paper, we use the SIFT feature descriptors to represent image patches. An image patch centered at the selected key point $\mathbf{p}(x, y, s, \theta)$ with width of $6 \cdot s + 1$ pixels is divided into 4×4 small adjacent regions. The image gradient magnitudes and orientations of each pixel are calculated in the patch. Each

region is described by 8-bin histogram of gradients representing the gradient magnitude of 8 main directions angles. In an image patch, 4×4 histograms of gradients are connected as feature vector $\mathbf{f}(\mathbf{p}(x, y, s, \theta))$ (dimension=128).

2.1.3 Support Vector Regressor

The regressive support vector machine a.k.a. SVR or RSVM has been well developed since last century. Suppose we are given training data $\{(\mathbf{f}_1, \mathbf{d}_1), (\mathbf{f}_2, \mathbf{d}_2) \dots (\mathbf{f}_n, \mathbf{d}_n)\}$ $\mathbf{f} \in \mathbb{R}^{d=128}$. In ε -SV regression, our goal is to find a function $\delta(\mathbf{f})$ that has at most ε deviation from the actually obtained targets \mathbf{d}_j for all the training data, and at the same time it is as flat as possible. SVR is capable of dealing with nonlinear problems using a Gaussian RBF kernel. The detail of SVR is elaborated in [27].

2.1.4 Displacement Normalization and Denormalization

Displacement normalization is the key point of Rotation-Invariant Regression Voting. In each stage of training, for each landmark $L_i(x, y), i = 1, 2, 3, 4, N$ random image patches $\mathbf{p}_j(x, y, s, \theta), 1 \leq j \leq N$ is sampled in ROI, where the ROI is the whole radiograph in the first stage of RIRV or neighborhood of the landmarks in the latter stages. The displacements $\mathbf{d}_j(x, y)$ from the center of random patches to the ground truth of the landmark are calculated. Then, the normalized displacement $\mathbf{d}^{norm}_j(x^{norm}, y^{norm})$ is calculated as:

$$\mathbf{d}^{norm}_j(x^{norm}, y^{norm}) = \begin{bmatrix} x^{norm} \\ y^{norm} \end{bmatrix} = \frac{\text{rotate}(\mathbf{d}_j(x, y), \theta_j)}{s_j}, \quad (1)$$

$$\text{rotate}(\mathbf{d}(x, y), \theta) = \begin{bmatrix} \cos(\theta) & -\sin(\theta) \\ \sin(\theta) & \cos(\theta) \end{bmatrix} * \begin{bmatrix} x \\ y \end{bmatrix} \quad (2)$$

where $\text{rotate}(\cdot)$ means rotate a vector by θ degree. After normalization, \mathbf{d}^{norm}_j is in the coordinate of corresponding \mathbf{p}_j relative to both orientation θ_j and scale s_j .

In each stage of prediction, $\mathbf{d}^{norm}_j(x^{norm}, y^{norm})$ predicted by SVR regressor is denormalized to $\mathbf{d}_j(x, y)$ as:

$$\mathbf{d}_j(x, y) = \begin{bmatrix} x^{norm} \\ y^{norm} \end{bmatrix} = \text{rotate}(\mathbf{d}^{norm}_j(x^{norm}, y^{norm}), -\theta_j) * s_j \quad (3)$$

where $\mathbf{d}_j(x, y)$ is in origin coordinate of whole image.

The normalization and denormalization can be illustrated in Figure 5, where red arrows and green arrows represent image coordinate and patch coordinate, respectively. Though the displacements $\mathbf{d}_j(x, y)$ in image coordinates are different in two images, the displacements $\mathbf{d}^{norm}_j(x^{norm}, y^{norm})$ in its corresponding patch coordinates are the same.

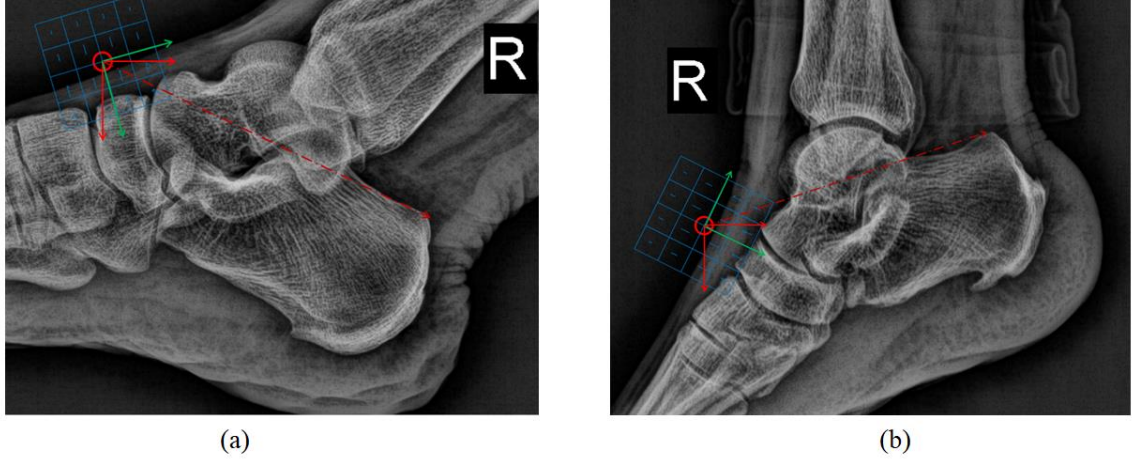


Figure 5 Displacement normalization in calcaneus radiograph. (a) Radiograph 1. (b) Radiograph 2. Blue squares represent SIFT patches at a specific anatomical location. Green and red arrows are the patch-based coordinates and image coordinates, respectively. Crimson dash lines are the displacements from the centers of patches to L_1 .

2.1.5 Procedures of RIRV

In training of RIRV method, we employed multi-stage coarse-to-fine strategy with four stages. In each stage, for each landmark $L_i(x, y)$, $i = 1, 2, 3, 4$, we train a support vector regressor $\delta_{h,i} = [\delta_{h,i}^x; \delta_{h,i}^y]$ by the set of N pairs $\{(\mathbf{d}_j^{norm}, \mathbf{f}_j)\}$ sampled randomly in the ROI, where h is the number of stage. For the first stage, ROI is the whole radiograph. For the other stages, the ROI is the neighborhood of $L_i(x, y)$. The width of each ROI is $D_{roi;h}$ pixels, where h is the number of stage. The orientation θ of image patch is automatically assigned by the dominant gradient angle in the patch according to SIFT [28] in the first stage. In the latter stages, θ is the slope angle of line $L_1 - L_3$ obtained from the previous stage with random perturbing $[\Delta\theta_{min;h}, \Delta\theta_{max;h}]$ to make use of the rotation information of the coarse detection. The scale of the patch is randomly and flatly assigned in range in $[s_{min;h}, s_{max;h}]$ where h is the number of stage. A higher range of scale contributes to scale-invariance.

Before training, all radiographs are horizontally flipped to toe-left because SIFT feature has no symmetrical invariance. In the prediction, toe-left and toe-right can be automatically identified and transformed to toe-left as well.

The prediction of RIRV is the proper reverse of training. In each stage, for each landmark $L_i(x, y)$, $i = 1, 2, 3, 4$ we use $\delta_{h,i} = [\delta_{h,i}^x; \delta_{h,i}^y]$ to predict $\bar{\mathbf{d}}_j^{norm} = \delta_{h,i}(\mathbf{f}_j)$ with N \mathbf{f}_j sampled randomly in the ROI. Then we denormalize $\bar{\mathbf{d}}_j^{norm}$ to $\bar{\mathbf{d}}_j$. The voting candidates can be calculated as $\mathbf{c}_j = \mathbf{p}_j + \bar{\mathbf{d}}_j$. The image patch parameters $[\Delta\theta_{min;h}, \Delta\theta_{max;h}]$, $[s_{min;h}, s_{max;h}]$ and $D_{roi;h}$ should ensure that the image patches in prediction are less variant than in training (e.g. the scale range in prediction should be smaller than training).

In the prediction, we proposed a screening method named Half-Path Double Voting (HPDV) to remove unconfident voting candidates caused by far, noisy or blurry image patches. For each image patch \mathbf{p}_j in the first three prediction stage, a half-path patch $\mathbf{p}_j^{half}(x^{half}, y^{half}, s, \theta)$ is sampled at the midpoint

between voting candidate \mathbf{c}_j and the center of \mathbf{p}_j . The location of \mathbf{p}_j^{half} is calculated as $[x^{half}; y^{half}] = \mathbf{p}_j + \bar{\mathbf{d}}_j/2$. The half-path patch will operate a second voting by the same method to calculate \mathbf{c}_j^{half} . The result of \mathbf{c}_j^{half} is valid as final voting candidates \mathbf{c}_j^{valid} of the stage as:

$$\mathbf{c}^{valid} = \{\mathbf{c}^{half} \mid \|\mathbf{c}_j^{half} - \mathbf{c}_j\| < Th_h\} \quad (4)$$

where Th_h is the pixel deviation threshold empirically assigned to each stage. This method can be seen as a screening method to validate whether each voting candidate is credible. An example of HDPV is illustrated in Figure 6, where \mathbf{c} is denoted as green point and \mathbf{c}^{valid} is denoted as red point. The possibility density map obtained by Kernel Density Estimation (KDE) of \mathbf{c} and \mathbf{c}^{valid} are illustrated by Figure 6.(b) and Figure 6.(c), respectively. It can be seen that \mathbf{c}^{valid} is more concentrated and accurate. The voted landmarks location \bar{L}_i is located at the highest possibility in the density map.

In the prediction, all radiographs should be horizontally flipped to toe-left. Toe-direction can be automatically identified by a tentative prediction of L_1 in first stage in a flipped image pair as shown in Figure 7. The set of \mathbf{c}^{valid} performs lower deviation in toe-left than toe-right image because the regressor is trained with toe-left images. A prediction in toe-right image would fail and result in far less \mathbf{c}^{valid} with high deviation. Thus, toe-direction can be indirectly told by the standard deviation of voting candidates in the flipped image pair. The flowchart of RIRV landmark detection method is shown in Figure 8.

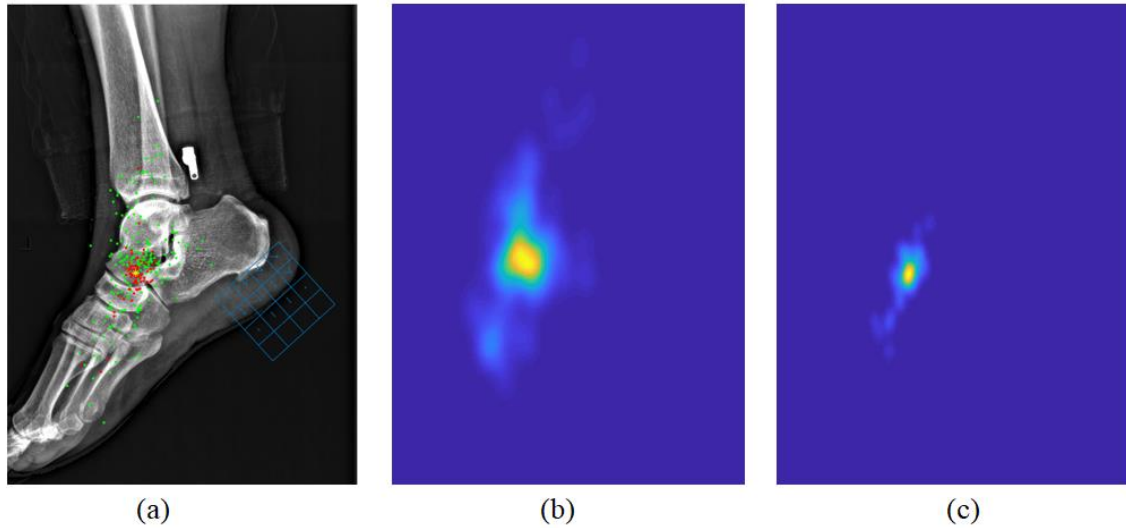


Figure 6 Half-Path Double Voting in RIRV. (a) Voting result on radiograph. Original voting candidates \mathbf{c} are denoted as green point and screened valid candidates \mathbf{c}^{valid} are denoted as red point. (b) The heat map of \mathbf{c} . (c) The heat map of \mathbf{c}^{valid} .

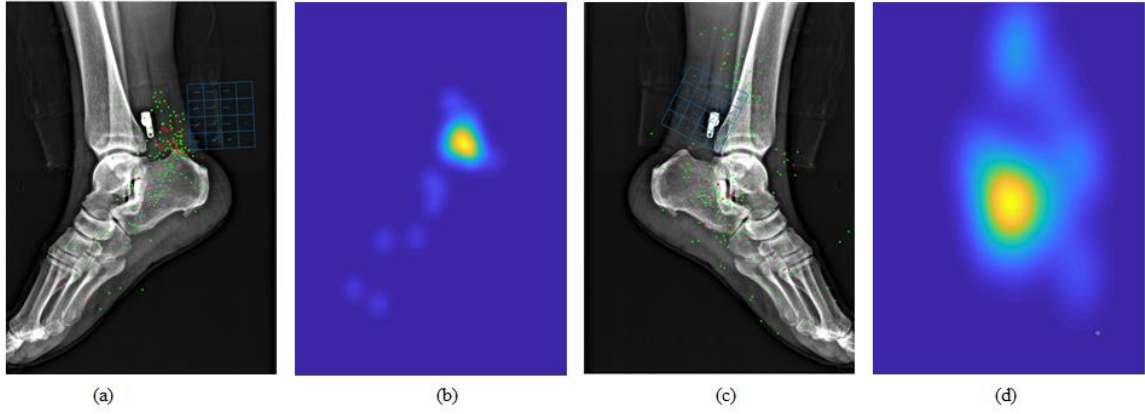


Figure 7 Left-Right Identification. (a) Tentative prediction in toe-left radiograph. (b) The heat map of c^{valid} in toe-left radiograph. (c) Tentative prediction in toe-right radiograph. (d) The heat map of c^{valid} in toe-right radiograph.

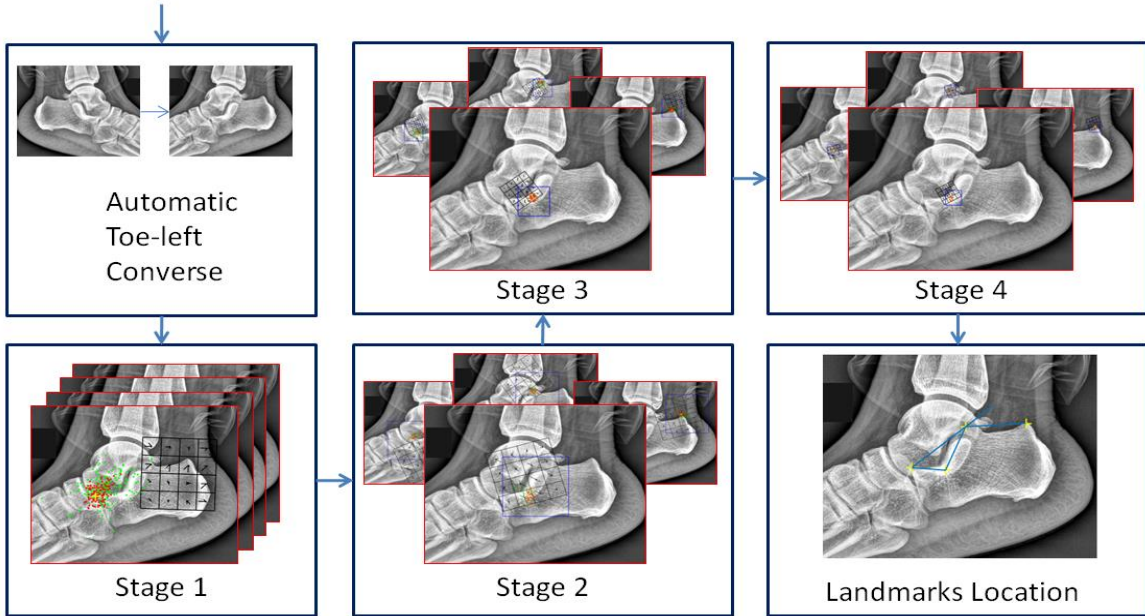


Figure 8 Flow chart of landmark detection in lateral calcaneus radiograph based on RIRV

2.2 Bohler's and Gissane's Angle Calculation

After four landmarks are located, the anatomical angles can be measured. The Bohler's Angle is calculated by:

$$\angle BA = 180^\circ - \angle L_1 L_2 L_3 = \frac{A \cdot B}{\|A\| * \|B\|} * \text{sign}(A \times B) * \frac{180}{\pi}, \quad (5)$$

$$\begin{cases} A = L_2 - L_3 \\ B = L_1 - L_2 \end{cases} \quad (6)$$

where $\angle L_1 L_2 L_3$ is the angle beneath vertex L_2 ; $\text{sign}(\cdot)$ gives the sign in the parentheses, which means $\angle L_1 L_2 L_3$ can also be a reflex angle and $\angle BA$ can be negative. The Critical Angle Gissane is calculated by:

$$\angle CAG = \angle L_2 L_4 L_3 = \frac{(L_2 - L_4) \cdot (L_3 - L_4)}{\|L_2 - L_4\| * \|L_3 - L_4\|} * \frac{180}{\pi}. \quad (7)$$

2.3 Fracture Identification based on Multi-Stream CNN

Convolution neural network has been well performed in medical image processing since the breakthrough of AlexNet. The default CNN architecture can easily accommodate multiple sources of information or representations of the input, in the form of channels presented to the input layer [29]. The multi-stream multi-scale architecture was first explored by Farabet et al. (2013) for multi-scale image analysis and 2.5D classification. Several medical applications have successfully used this concept [30] [31].

In this section, we designed a multi-stream CNN to classify calcaneal fracture taking advantage of the landmarks location predicted from RIRV. For the preprocessing, the radiograph is converted to toe-left and rotated to L_1 - L_3 horizontal. Then, ROI is cropped based on the location of the landmarks: ROI1 is the anterior calcaneus between L_3 and L_2 , ROI2 is the posterior calcaneus between L_2 and L_1 and ROI3 contains whole calcaneus. Each ROI serves as the input of one stream of the multi-stream CNN. Each stream is one classical pre-trained Inception-v3 [32] ending by a full connection (FC) layer of 1024 nodes. The last FC layers of three stream are concatenated and followed by 1024 nodes FC layer and classification output. The layout of multi-stream CNN and preprocessing is illustrated in Figure 9. By normalizing the region of interest in accordance to the location of the landmarks, the CNN can look closer to the feature of fracture instead of deal with other trivial information, like rotation and view.

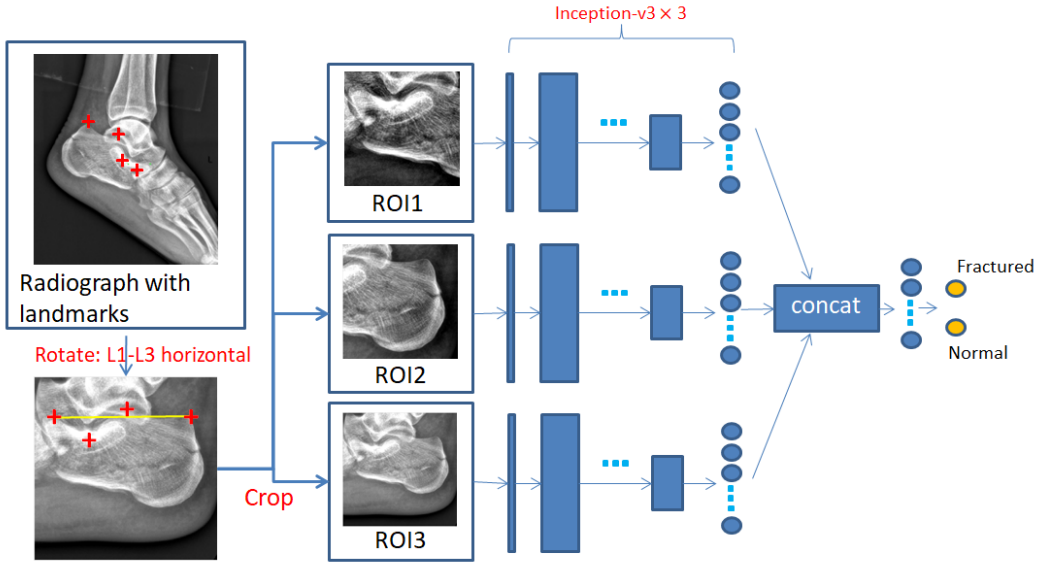


Figure 9 Layout of multi-stream CNN and input preprocessing

3 Experiments and Results

3.1 Experimental Dataset

We evaluated the proposed approach on the calcaneal radiograph dataset collected from two hospitals: Huludao Central Hospital and Liaoning Fuxin Hospital. For evaluation, four landmarks were manually annotated by experienced orthopedists and judgments of fracture were made. The dataset includes 630 radiographs of normal calcaneus, 184 radiographs of fractured calcaneus (87 intra-articular tongue-type,

64 intra-articular joint-depression and 33 extra-articular) and 91 radiographs of suspicious fractured calcaneus. The image resolutions vary from 536×556 to 2969×2184 pixels.

In evaluation of RIRV, one fourth of the radiographs are separated as test set and the others for training set. In evaluation of multi-stream CNN, we test the algorithm by four-fold cross validation. There is no pixel-mm ratio annotated in radiograph, so we set the distance between L_1 and L_3 as a reference length to evaluate detection performance in millimeter. We assume the distance between L_1 and L_3 as 70mm and there is no prominent difference across individuals.

3.2 Evaluation of RIRV

3.2.1 Experimental Settings

The image patch parameters of RIRV in training and prediction are set as shown in Table 1 and Table 2 respectively. The values of parameters ensure that the image patches in prediction is less versatile and fickle than in training. In training SVR, we optimized the regression sensitivity ϵ , the kernel scale γ and the slack variable (box constrain) C independently from the test set.

Table 1 Image patch parameters in training

	$[\Delta\theta_{min}; h, \Delta\theta_{max}; h]$	$[s_{min}; h, s_{max}; h]$	$D_{roi; h}$	N
Stage One(h=1)	N/A	[30,50]	N/A	100
Stage Two(h=2)	$[-\pi/4, \pi/4]$	[20,40]	440	100
Stage Three(h=3)	$[-\pi/6, \pi/6]$	[10,20]	300	80
Stage Four(h=4)	$[-\pi/6, \pi/6]$	[7,10]	200	50

Table 2 Image patch parameters in prediction

	$[\Delta\theta_{min}; h, \Delta\theta_{max}; h]$	$[s_{min}; h, s_{max}; h]$	$D_{roi; h}$	N	Th_h
Stage One(h=1)	N/A	[30,50]	N/A	200	100
Stage Two(h=2)	$[-\pi/6, \pi/6]$	[25,35]	300	100	60
Stage Three(h=3)	$[-\pi/12, \pi/12]$	[10,20]	160	80	30
Stage Four(h=4)	$[-\pi/12, \pi/12]$	[8,9]	80	50	N/A

3.2.2 Evaluation Criterion

The first evaluation criterion is Mean Radius Error (MRE) associated with Standard Deviation (SD) of the four landmarks and Mean Angle Error (MAE) of two anatomical angles. The Radial Error (RE) is the distance between the predicted position and the annotated true position of each landmark. The Angle Error (AE) is the absolute difference between the angles calculated by predicted landmarks and annotated landmarks. The MRE, SD and MAE are defined as:

$$MRE = \frac{\sum_{i=1}^M RE_i}{N}, \quad (8)$$

$$SD = \sqrt{\frac{\sum_{i=1}^M RE_i - MRE}{N-1}}, \quad (9)$$

$$MAE = \frac{\sum_{i=1}^M AE_i}{N}, \quad (10)$$

where N is the total number of radiographs in test set. Another criterion is the Success Detection Rate (SDR) with respect to 2mm, 3mm and 6mm. If RE_i is less than a precision range, the detection of the scale is considered as a successful detection in the precision range; otherwise, it is considered as a failed detection. The SDR with Real Length Error less than error precision p is defined as:

$$SDR_p = \frac{\{RE_i < p\}}{N} \times 100\%, 1 \leq i \leq N, \quad (11)$$

where p denotes the three precision range: 2mm, 3mm and 6mm

3.2.3 Experimental Result

Experimental results of calcaneal landmarks detection are shown in Table 3. The average MRE and SD of four landmarks in all radiographs are 1.85 and 1.61mm, respectively. The results of calcaneal angle measurements are shown in Table 4.

Comparison between our proposed RIRV with a state-of-art landmark detection method MDTRV [11](multiresolution decision tree regression voting) is shown in Table 5. The MDTRV is a regression-voting based method tested on cephalogram database of 2015 ISBI Challenge with an equivalent or better performance than RFRV-CLM [10] and [21]. Furthermore, we train our method by non-augmented training set but test it on an augmented test set, in which all radiographs were randomly rotated (up to 360°) in order to prove the explicit rotation-invariance character of RIRV. The result is shown in Table 5 headed with RIRV-RTS (rotated test set).

The result shows that our methods outperformed MDTRV, especially in terms of standard deviation. The high SD of MDTRV is mainly caused by the complete misdetection of some radiographs with great rotation that seldom appears in training set. In addition, there is no prominent difference in the result of RIRV between original and rotated test set.

Table 3 Statistical results of landmark detection

	MRE(mm)	SD(mm)	SDR_2mm(%)	SDR_4mm(%)	SDR_6mm(%)
L_1	1.05	0.90	88.84	98.76	99.59
L_2	2.73	2.22	47.11	78.51	92.15
L_3	1.73	1.63	68.18	95.87	97.93
L_4	1.92	1.69	64.88	92.98	96.28
Average	1.85	1.61	67.25	91.53	96.49

Table 4 Statistical results of calcaneal angles measurements

	MAE(°)	SD(°)
BA	3.84	4.20
CAG	6.19	6.23

Table 5 Comparison between RIRV with MRDTV in original test set and RIRV in randomly rotated test set

	MRE(mm)	SD(mm)	SDR_2mm(%)	SDR_4mm(%)	SDR_6mm(%)
MRDTV	3.25	11.07	62.31	86.63	90.15
RIRV(Ours)	1.85	1.61	67.25	91.53	96.49
RIRV-RTS	1.87	1.72	68.88	91.32	97.01

3.3 Evaluation of Multi-stream CNN

The inputs of multi-stream CNN are stacks of three images; each image of one stack is a region of calcaneus cropped from a radiograph according to the landmarks detected by RIRV. The image is resized to $299 \times 299 \times 3$ to align with the original input of Inception-v3. The training labels of the image stacks are the annotated labels of the corresponding radiographs: normal or fractured. The suspicious fractured radiographs are labeled as fractured in training to increase sensitivity but discarded in test due to difficulty of evaluation. There is no subdivided fracture type during training and test, but the binary classification sensitivity is analyzed within each fracture type.

Each stream of our CNN is an Inception-v3 net pre-trained on a subset of ImageNet from ImageNet Large-Scale Visual Recognition Challenge (ILSVRC) [33]. The classification layers of the pre-trained CNNs are discarded and concatenated by a full connection (FC) layer of 1024 nodes with random initial weights. The layers of the network are trained with global initial learning rate of 0.002 and a drop factor of 0.8 every 5 epochs. We use RMSProp optimizer with a decay factor of 0.999, momentum of 0.9 and epsilon of $1e-8$. We use MATLAB deep learning package to train, validate and test our method. During training, images are augmented with random rotation between -10° and $+10^\circ$ and random translation within 30 pixels; there is no random flip. The augmentation is limited to low extent in order to maintain the normalized information resulted from multi-region image cropping.

The trained CNN can output a continuous number between 0 and 1 as the possibility of fracture in the image. Performance curve can be plotted by sensitivity vs 1-specificity when varying the decision threshold and area under curve (AUC) can be calculated as evaluation criterions. Sensitivity and specificity are defined as:

$$\text{sensitivity} = \frac{\text{true positive}}{\text{positive}} \quad (12)$$

$$\text{specificity} = \frac{\text{true negative}}{\text{negative}} \quad (13)$$

where true positive, positive, true negative and negative are the number of correctly predicted fractured radiographs, fractured radiographs in test set, correctly predicted normal radiographs and normal radiographs in test set, respectively.

We compare our method with several mainstream CNNs including GoogLeNet, VGG19, Inception-v3 and Resnet101. All baseline CNNs are trained and tested on the normalized whole calcaneus image, i.e. ROI3 in Figure 9. Performance curves are plotted in Figure 10. The sensitivities of overall fracture, intra-articular fracture and extra-articular fracture are shown in Table 6, giving a specificity of 95% in performance curve. The result shows that our method outperforms all baseline CNNs, especially in range of specificity higher than 90%.

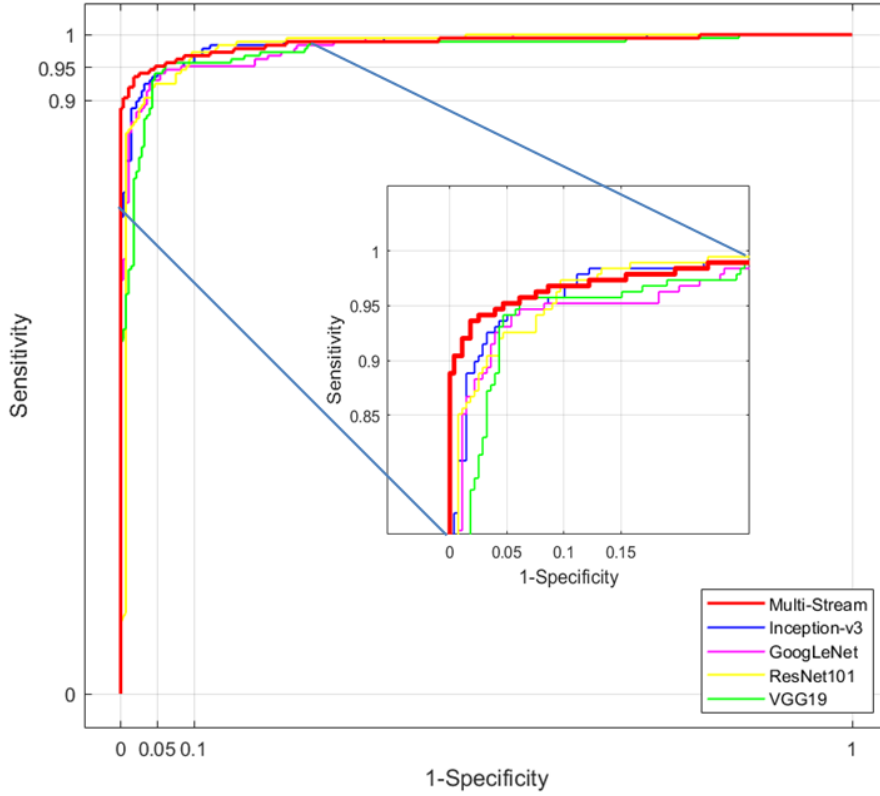


Figure 10 Performance curve of the tested CNN.

Table 6 Statistical comparison of fracture identification

Networks	AUC	Specificity	Sensitivity at giving Specificity		
			Overall	Intra-articular	Extra-articular
VGG19	0.975		94.15%	97.32%	81.82%
Resnet101	0.982		92.55%	96.64%	75.76%
Inception-V3	0.985	95.32%	93.62%	97.99%	75.76%
GoogLeNet	0.982		93.09%	97.99%	72.73%
Multi-Stream	0.988		95.21%	98.66%	81.82%

4 Discussion

The result shows that we can build a calcaneal radiograph analysis system including anatomical angles measurement and fracture identification. The proposed RIRV landmark detection method is suitable for calcaneal landmark detection for its explicit rotation-invariant characteristic. The approach can deal with 360° rotation of image without of training augmentation. We randomly selected a subset of 20 in the dataset, asking two experienced clinicians to manually annotate the four landmarks in order to calculate inter-observer variability. The inter-observer MRE and SD between two observers are 1.53mm and 1.39mm, respectively. The inter-observer MAE of BA and CAG is 2.21° and 4.95° . The result shows that our proposed algorithm can achieve MRE of 1.85mm and SD of 1.61mm, which means that RIRV is a little bit poorer than manual annotation but still satisfactory. The detection accuracy of landmarks and angels varies from one to another; L_1 shows good accuracy while L_2

shows the worst. There are three main reasons. First, L_2 and L_4 are sometimes not imaged clearly because they are blocked by overlaying tarsus. Second, the definition of L_2 , i.e. the apex of the posterior facet of the calcaneus, is hard to precisely carried out in annotating because posterior facet is an arc and its apex is widely ranged. Third, in fractured calcaneus radiograph, the anatomical structure of landmarks, especially for L_2 and L_3 , is changed by fracture of calcaneus, and the feature varies from one fractured instance to another. The accuracy of CAG is poor than BA; however, the analysis as well as literatures [34] shows that inter-observer variability for CAG is poor as well. Though statistical shape model is needless in our method due to small number of landmarks, RIRV as independent localizers, can be easily integrated with ASMs and CLMs.

The proposed multi-stream CNN structure can help to screen fractured calcaneus. Due to the ROI normalization by prior information i.e. the location of landmarks, the proposed CNN architecture could deal with the subtle feature of different fractures, presenting good performance with AUC of 0.988 and sensitivity of 95.21% giving 95% specificity. The sensitivity of extra-articular fracture is far lower than intra-articular because of its trivial feature. In addition, the approach does not involve axial and oblique radiographs so far; therefore, fractures that can only be identified from other angles are hard to be detected in our method. The system performs binary classification to identify whether fracture or not but prediction and localization of the type of fracture are not investigated yet, so the system only servers as a screening tool.

5 Conclusion

In conclusion, we proposed a calcaneal radiograph analysis system, which contained anatomical angle measurement and fracture identification. The system solved the fickle rotation of calcaneus in radiographs by a Rotation-Invariant Regressive-Voting (RIRV) landmark detection approach. And the explicit rotation-scale invariance it contained came from a novel normalization method. The experimental result presented the mean radius error of landmarks of 1.85mm and mean error of Bohler's Angle of 3.8°. The equivalent performance on randomly rotated test set proves its rotation-invariant characteristic. We also designed a multi-stream CNN composed of three paralleled Inception-v3 concatenated to single classification output. The network was trained by stacks of three ROIs cropped and normalized from calcaneal radiographs, according to the landmarks which were detected by RIRV. The proposed CNN architecture could deal with the subtle feature of different fractures, presenting good performance with AUC of 0.988 and sensitivity of 95.21% giving 95% specificity. In the future, a system using lateral, axial and oblique calcaneus radiographs can be built using multi-stream CNN. We will further develop the system to detect the location of the fracture and classify the fine-grained fracture type.

Declarations of interest

The authors declare that there are no conflicts of interest regarding the publication of this paper.

Reference

- [1] Daftary, Aditya, Andrew H. Haims, and Michael R. Baumgaertner. "Fractures of the calcaneus: a review with emphasis on CT." *Radiographics* 25.5 (2005): 1215-1226.
- [2] Böhler, Lorenz. "Diagnosis, pathology, and treatment of fractures of the os calcis." *JBJS* 13.1

(1931): 75-89.

- [3] Sanders, Roy. "Current concepts review-displaced intra-articular fractures of the calcaneus." *JBJS* 82.2 (2000): 225-50.
- [4] Crawford, Haemish A, C. G. Walker, and M. J. Boyle. "The paediatric Bohler's angle and crucial angle of Gissane: a case series." *Journal of Orthopaedic Surgery & Research* 6.1(2011):2.
- [5] Di Schino, M., et al. "Results of open reduction and cortico-cancellous autograft of intra-articular calcaneal fractures according to Palmer." *Revue de chirurgie orthopedique et reparatrice de l'appareil moteur* 94.8 (2008): e8-e16.
- [6] Cave, Edwin F. "7 Fracture of the Os Calcis-The Problem in General." *Clinical Orthopaedics and Related Research (1976-2007)* 30 (1963): 64-66.
- [7] Hildebrand, KEVIN A., et al. "Functional outcome measures after displaced intra-articular calcaneal fractures." *The Journal of bone and joint surgery. British volume* 78.1 (1996): 119-123.
- [8] Lamarre, Marie-Eve, et al. "Assessment of spinal flexibility in adolescent idiopathic scoliosis: suspension versus side-bending radiography." *Spine* 34.6 (2009): 591-597.
- [9] Fakhrai, Negar, et al. "Automatic assessment of the knee alignment angle on full-limb radiographs." *European journal of radiology* 74.1 (2010): 236-240.
- [10] C. Lindner, C.-W. Wang, C.-T. Huang et al., "Fully automatic system for accurate localisation and analysis of cephalometric landmarks in lateral cephalograms," *Scientific Reports*, vol. 6, no. 1, 2016.
- [11] S. Wang, H. Li, J. Li, Y. Zhang and B. Zou, "Automatic Analysis of Lateral Cephalograms Based on Multiresolution Decision Tree Regression Voting", *Journal of Healthcare Engineering*, vol. 2018, pp. 1-15, 2018.
- [12] Donner, René et al. "Localization of 3D anatomical structures using random forests and discrete optimization." *International MICCAI Workshop on Medical Computer Vision*. Springer, Berlin, Heidelberg, 2010.
- [13] Pauly, Olivier, et al. "Fast multiple organ detection and localization in whole-body MR Dixon sequences." *International Conference on Medical Image Computing and Computer-Assisted Intervention*. Springer, Berlin, Heidelberg, 2011.
- [14] C. Lindner and T. F. Cootes, "Fully automatic cephalometric evaluation using random forest regression-voting," in *Proceedings of International Symposium on Biomedical Imaging (ISBI), Grand Challenges in Dental X-ray Image Analysis—Automated Detection and Analysis for Diagnosis in Cephalometric X-ray Image*, Brooklyn, NY, USA, May 2015.
- [15] Yang, Dong, et al. "Automated anatomical landmark detection on distal femur surface using convolutional neural network." *2015 IEEE 12th international symposium on biomedical imaging (ISBI)*. IEEE, 2015.
- [16] de Vos, Bob D., et al. "2D image classification for 3D anatomy localization: employing deep convolutional neural networks." *Medical Imaging 2016: Image Processing*. Vol. 9784. International Society for Optics and Photonics, 2016.
- [17] J. Gall and V. Lempitsky, "Class-specific Hough Forests for object detection," in *Proc. Comput. Vis. Pattern Recognit.*, 2009, pp. 1022–1029.
- [18] L. Breiman, "Random Forests," *Mach. Learn.*, vol. 45, pp. 5–32, 2001. M. Valstar, B. Martinez, X. Binefa, and M. Pantic, "Facial point detection using boosted regression and graph models," in *Proc. Comput. Vis. Pattern Recognit.*, 2010, pp. 2729–2736.
- [19] T. Cootes, M. Ionita, C. Lindner, and P. Sauer, "Robust and accurate shape model fitting using Random Forest regression voting," in *Proc. ECCV 2012—Part VII*, Springer LNCS #7578, 2012,

- pp. 278–291.
- [20] R. Donner, B. Menze, H. Bischof, and G. Langs, "Global localization of 3D anatomical structures by pre-filtered Hough Forests and discrete optimization, " *Med. Image Anal.*, vol. 17, no. 8, pp. 1304–1314, 2013.
 - [21] Reddy, B. Srinivasa, and Biswanath N. Chatterji. "An FFT-based technique for translation, rotation, and scale-invariant image registration." *IEEE transactions on image processing* 5.8 (1996): 1266-1271.
 - [22] R. Vandaele, J. Aceto, M. Muller et al., "Landmark detection in 2D bioimages for geometric morphometrics: a multiresolution tree-based approach," *Scientific Reports*, vol. 8, no. 1, 2018.
 - [23] Roth, Holger R., et al. "Deep convolutional networks for automated detection of posterior-element fractures on spine CT." *Medical Imaging 2016: Computer-Aided Diagnosis*. Vol. 9785. International Society for Optics and Photonics, 2016.
 - [24] Wu, Jie, et al. "Fracture detection in traumatic pelvic CT images." *Journal of Biomedical Imaging* 2012 (2012): 1.
 - [25] Rahmaniari, Wahyu, and Wen-June Wang. "Real-Time Automated Segmentation and Classification of Calcaneal Fractures in CT Images." *Applied Sciences* 9.15 (2019): 3011.
 - [26] Pranata, Yoga Dwi, et al. "Deep learning and SURF for automated classification and detection of calcaneus fractures in CT images." *Computer methods and programs in biomedicine* 171 (2019): 27-37.
 - [27] Alex J. Smola†, and Bernhard Schoölkopf‡. "A Tutorial on Support Vector Regression*." *Statistics and Computing* 14.3(2004):199-222.
 - [28] D. Lowe, "Distinctive Image Features from Scale-Invariant Keypoints", *International Journal of Computer Vision*, vol. 60, no. 2, pp. 91-110, 2004.
 - [29] Litjens, Geert, et al. "A survey on deep learning in medical image analysis." *Medical image analysis* 42 (2017): 60-88.
 - [30] Kamnitsas, Konstantinos, et al. "Efficient multi-scale 3D CNN with fully connected CRF for accurate brain lesion segmentation." *Medical image analysis* 36 (2017): 61-78.
 - [31] Song, Youyi, et al. "Accurate segmentation of cervical cytoplasm and nuclei based on multiscale convolutional network and graph partitioning." *IEEE Transactions on Biomedical Engineering* 62.10 (2015): 2421-2433.
 - [32] Szegedy, Christian, Vincent Vanhoucke, Sergey Ioffe, Jon Shlens, and Zbigniew Wojna. "Rethinking the inception architecture for computer vision." In *Proceedings of the IEEE Conference on Computer Vision and Pattern Recognition*, pp. 2818-2826. 2016.
 - [33] Russakovsky, O., Deng, J., Su, H., et al. "ImageNet Large Scale Visual Recognition Challenge." *International Journal of Computer Vision (IJCV)*. Vol 115, Issue 3, 2015, pp. 211–252
 - [34] Otero, Jesse E., et al. "There is poor reliability of Böhler's angle and the crucial angle of Gissane in assessing displaced intra-articular calcaneal fractures." *Foot and Ankle Surgery* 21.4 (2015): 277-281.